**ORIGINAL PAPER**

# Stainless steel supported NiS/CeS nanocomposite for significantly enhanced oxygen evolution reaction in alkaline media

Abdul Ghafoor Abid[1] · Muhammad Faheem Ashiq[1] · Nada Alfryyan[2] · Sumaira Manzoor[1] · Mehar Un Nisa[1] ·
M. S. Al-Buriahi[3,4] · Sultan Alomairy[5] · Z. A. Alrowaili[6] · Muhammad Naeem Ashiq[1]

## Abstract

The discovery of highly active and cost-effective materials capable of catalyzing the oxygen evolution reaction (OER) is essential for water splitting. In the present study, we developed a new method for producing the structural components of advanced non-precious metal electrocatalysts NiS/CeS nanocomposite supported on stainless steel strip (SSS) represented as NiS/CeS/SSS that are both innovative and practical. To accomplish a current density of 10 mA cm$^{-2}$, the NiS/CeS/SSS requires OER overpotential of 289 mV, which is smaller than the pure NiS/SSS (319 mV) and CeS/SSS (309 mV), and with enhanced stability of 40 h tested in 1.0 M KOH electrolyte. The higher efficiency of OER is due to the strong electrical contacts between NiS/SSS and CeS/SSS, the availability of active centers, and also the lower charge transfer resistance.

**Keywords** NiS/CeS/SSS nanocomposite · Stainless steel strip · Synergistic effect · Oxygen evolution reaction · Interface stability

## Introduction

One of the most important challenges today is finding additional energy resources with low-cost options for generating sustainable energy which is the main focus of the researchers [1–3]. Electrochemical water splitting is a low-cost, simple, and environment-friendly method for producing clean energy [4, 5]. In the long run, it can replace fossil fuels, making it a successful and necessary strategy. The oxygen evolution reaction (OER), which involves the transfer of four electrons and the production of different substances, gives electrochemical conversion cycles that use chemical fuels and renewable electricity the electrons they need. Electrical catalysts are important for making and breaking chemical bonds because they let electrons pass through [6, 7] due to the slow kinetics and simultaneous involvement of four electrons [8, 9]. OER catalysts are difficult to design due to sluggish kinetics; therefore, the researcher focus on advance, inexpensive, highly active electrocatalysts with small overpotential [10–12]. Hence, electrochemical water splitting electrodes were fabricated from various metal oxides and metal sulfides to achieve low overpotential and small Tafel slope [13–15]. Previously, industrial H2 was produced using natural gas, which consumed a large amount of nonrenewable energy and released carbon dioxide into the atmosphere. In recent years, electrochemical water separation has emerged as a feasible promise for low-cost, pollution-free, and energy-sustaining H2 generation. As a result, researchers worldwide have been attempting to create cost-effective and efficient electrochemical water splitting techniques such as bipolar water electrolysis, photovoltaic water splitting, solar cells, thermoelectric devices, and nano-turboelectric generators [16]. The focus of this study was the interaction of strongly polarized electronegative sulfur (such as CeS) with highly electropositive metals sulfides to achieve better

✉ Muhammad Naeem Ashiq
naeembzu@bzu.edu.pk

1  Institute of Chemical Sciences, Bahauddin Zakariya
   University, Multan 60800, Pakistan

2  Department of Physics, College of Science, Princess
   Nourah bint Abdulrahman University, P.O. Box 84428,
   Riyadh 11671, Saudi Arabia

3  Department of Physics, Sakarya University, Sakarya, Turkey

4  Physics Department, King Khalid University, P.O. Box 9004,
   Abha, Saudi Arabia

5  Physics Department, College of Science, Taif University,
   P.O. Box 11099, Taif 21944, Saudi Arabia

6  Department of Physics, College of Science, Jouf University,
   P.O. Box 2014, Sakaka, Saudi Arabia

efficiency [16, 17]. It will assist in removing electropositive and harmful ion residues during an electrochemical operation [18, 19]. Nickel- and cerium-based sulfides are inexpensive, safe, and effective electrocatalysts [20, 21] but both sulfides as individual has low chemical stability as well as low conductivity. By combining these two materials, i.e., NiS and CeS, it can improve the chemical stability as well as the conductivity due to their covalent interaction with sulfide and metal. The solvothermal technique, which maintains an adequate pressure and temperature balance, produces materials with exceptional quality having a wide range of morphologies [22–26]. Hence, the electrochemical stability of the system could be improved by mixing Ni-based sulfide with Ce-based derivatives due to their synergistic effect [27, 28]. Current research looks at the intriguing possibility of morphology-dependent electrochemical activity to increase electrochemical performance [29–32]. Hence, these issues can be solved by combining transition metal sulfides with other appropriate materials to form nanocomposites [33]. Zhang et al. [34] created tubular spheres of $(Fe_{0.2}Ni_{0.8})0.96S$ on Ni substrate to explore the complete kinetics of water splitting in both HER and OER. While working on iron-doped NiS nanoarrays, Qi et al. [35] and Sun et al. [36] employed this as an effective electrode for water splitting and described its long-term durability. Zhang et al. [37] published $(Ni,Fe)S_2@MoS_2$ electrocatalysts, and recognized the role of heterojunction in water splitting. Gong and his co-workers [38] explored water splitting in the OER and HER processes using manganese-doped $Cu_{7.2}S_4@NiS_2@NiS/NF$ electrocatalyst. According to Zheng's group, the electrocatalytic water splitting reaction of nickel sulfide nanostructures is phase-dependent. Srinivas et al. [39] and Wang et al. [40] developed $FeS_2/C$ nanocomposite as a general-purpose water splitting nanocomposite. Zhang et al. [41] also performed a study on water splitting electrocatalyst with a $NiS_2$ nanowire shape. To make thin $Ni_{0.8}Fe_{0.2}$ films, Nakayasu et al. [42] and Jing et al. [43] used hydrothermal electrodeposition and explained the process of OER. All the above-mentioned metal sulfide composites showed excellent stability as well as remarkable efficiency. From the above motivating concerns, we decided to prepare a one-step solvothermal synthesis for Ni- and Ce-based sulfide nanocomposite and compare the OER activity of NiS/SSS, CeS/SSS, and their nanocomposite electrodes already reported in literature.

Here in the present work, the used SSS is a common chemical engineering substrate due to its exceptional physical and chemical endurance in both basic and acidic environments making it a suitable choice for the present investigation. Additionally, such type of material has an extremely low electrical resistivity. The synthesized NiS/CeS/SSS was examined using XRD, SEM, TEM, BET, and XPS to determine its structure, morphology, surface area, and chemical composition, respectively. The cyclic voltammetry (CV), lin-

ear sweep voltammetry (LSV), electrochemical impedance spectroscopy (EIS), and chronoamperometric techniques were employed to evaluate the catalytic characteristics of the materials, and also the mechanism was studied using Tafel plots.

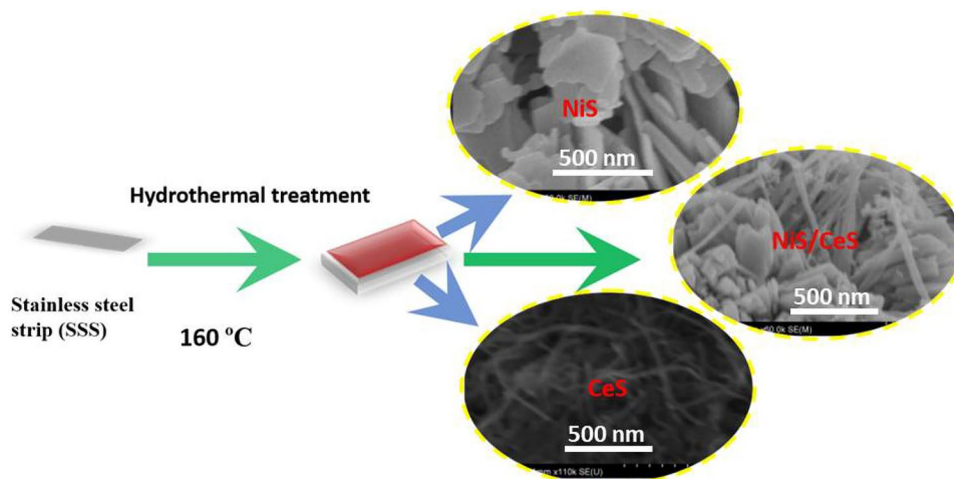# Experimental section

## Materials

The stainless steel strip (SSS) was provided by Kunshan Jiayisheng Electronics Co., Ltd. (thickness: 2000 mm, bulk density). Acetone, ethyl alcohol, nitric acid $(HNO_3)$, cerium nitrate hexahydrate $Ce(NO_3)_3.6H_2O$, nickel nitrate, hydrochloric acid (HCl), and thiourea $(H_2NCSNH_2)$ were provided by Sigma-Aldrich and Alfa Aesar. All chemicals were of interpretive grade, and the water utilized in sample preparation was ultrapure (deionized water) to ensure the quality of the produced materials.

## Synthesis of NiS/CeS/SSS nanocomposite

The stainless steel strip ($1*2$ cm$^2$) pieces were ultrasonically cleaned with acetone and hydrochloric acid, and it was necessary to rinse with an ethanol–water solution three times. A hydrothermal technique was used to fabricate NiS/CeS/SSS samples to achieve good morphology. For this purpose, the precursors like 0.5 mM $Ce(NO_3)_3.6H_2O$, 0.5 mM $Ni(NO_3)_2$, $6H_2O$, and 0.7 mM thiourea in 35 ml of deionized water were prepared and then stirred for 30 min. The resultant mixture and the pretreated SSS pieces were then poured into a 100 mL Teflon-lined stainless steel autoclave and reserved for heating at 160 °C for 12 h. After 12 h of treatment, the resulting system's temperature was naturally reduced to normal levels. It was continuously washed with deionized water and dehydrated in an oven overnight.

## Physical analysis

The PANanalytical X'Pert Pro device using Cu-Kα radiations was used to characterize the crystalline state and formation of the required phase of the synthesized nanostructured material. The morphology and size of the synthesized materials were studied using scanning electron microscopy with JSM-5600LV equipment at an accelerating voltage of about 80 kV. The electrochemical performance of the fabricated product was evaluated using a Mtrohm Autolab (PGSTAT-204) with a three-electrode cell setup. The working electrode was a synthesized material deposited on a stainless steel strip (SSS), with the counter and reference electrodes being an Ag/AgCl and a Pt filament, accordingly. The working electrode substrate was cleansed via micro-

cloth pads to remove the impurities present on the surface of the stainless steel strip, and then the SSS was subsequently cleaned with water and ethanol. The cleaned electrode was dried at 60 °C in a drying oven for 20 min, fabricated directly during hydrothermal treatment, and then employed for electrochemical experiments. The production, fabrication, and application of the nanocomposite nanostructure are depicted in Scheme 1.

All electrochemical studies, including linear sweep voltammetry (LSV), electrochemical impedance spectroscopy (EIS), cyclic voltammetry (CV), and chronopotentiometry, were executed by using a three-electrode electrochemical setup. The reference and counter electrodes for the catalyst-coated SSS working electrode were Ag/AgCl and platinum wire, respectively. We employed 1.0 M of potassium hydroxide (KOH) as an electrolyte during all electrochemical performances. A reversible hydrogen electrode with $V = 0.197 + 0.059 \times pH$ was used to set all potentials. At scanning rates of 5 mV s$^{-1}$, all the polarization curves of the electrocatalysts were investigated. The CV and LSV scans were used to calculate the Tafel slope by plotting the log of current density ($j$) versus overpotential ($\eta$). EIS was done between 100 kHz and 100 MHz at an applied potential of 0.5 V via a three-electrode system using Metrohm PGSTAT AUTOLAB-204.

## Result and discussion

### Structural, morphological, and textural analysis

Figure 1 represents the X-ray diffraction pattern of NiS, CeS, and NiS/CeS nanocomposite. Three strong peaks of NiS (Fig. 1) at around $2\theta = 30.192°$, 37.87°, and 69.80° were observed, which corresponds to the (300), (220), and (511) crystals plane indexed with the standard card JCPDS#

00–001-1286. Cell software was utilized to calculate the lattice parameters and found as $a = 9.815$ Å and $c = 2.853$ Å. The XRD pattern of the CeS has been well indexed with the standard card JCPDS # 00–004-0688, representing the diffraction peaks at 26.062°, 34.134°, 44.70°, 53.21°, 56.73°, 64.19°, and 73.74° that corresponds to the (111),
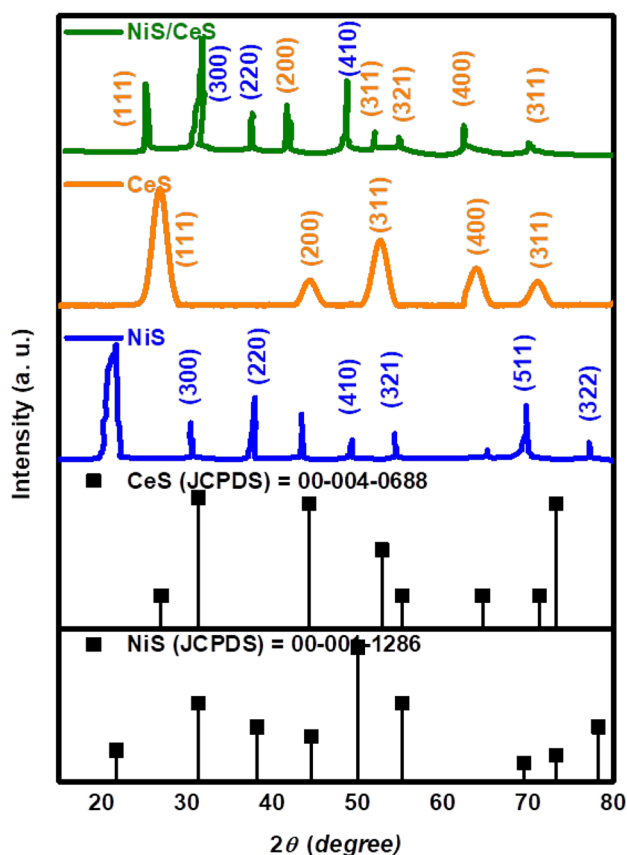


**Fig. 1** XRD pattern of all the synthesized products
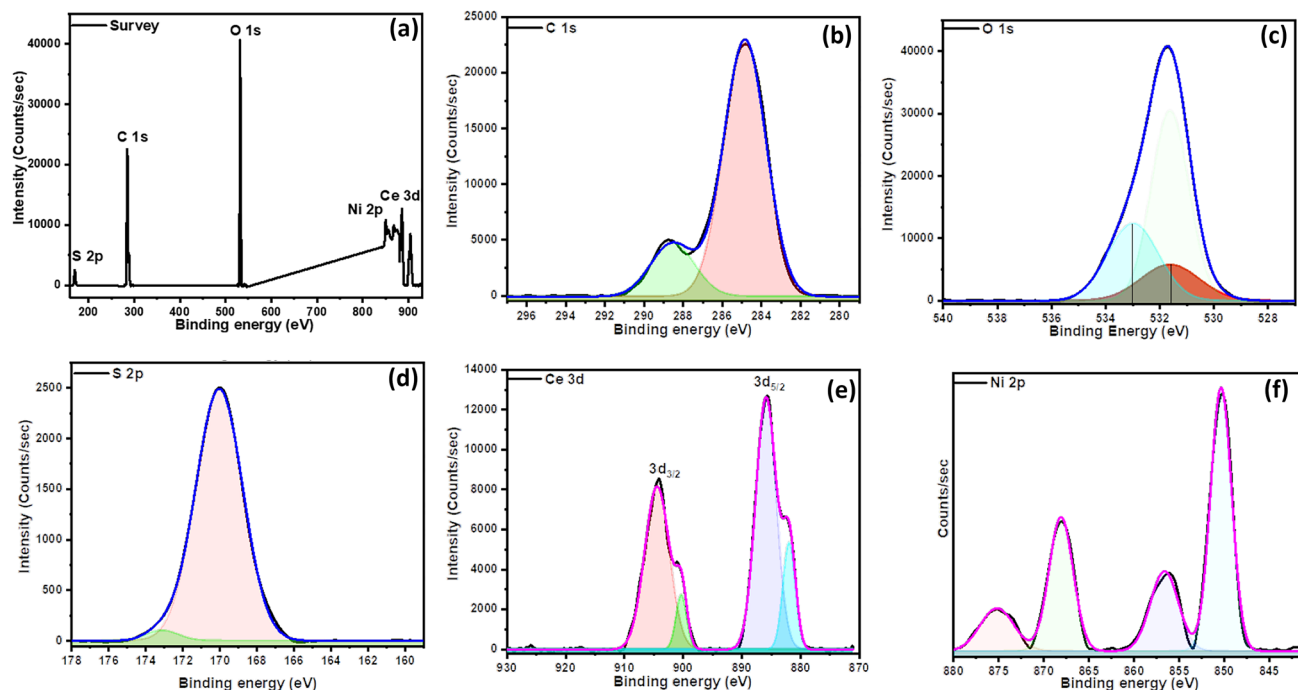
**Fig. 2** XPS. (**a**) Survey spectrum of composite, (**b**)=C 1 s, (**c**)=O 1 s, (**d**)=S 2p, (**e**)=Ce 3d, and **f**=Ni 2p

(200), (311), (222), (400), and (420) planes. On the other hand, the NiS/CeS composite has diffraction peaks of NiS and CeS with smaller fluctuations in intensity and 2-theta which may be due to the interaction between CeS and NiS, demonstrating that the composite material was synthesized successfully.

The valance states of the nanocomposite were evaluated using the XPS technique. The resultant nanocomposites survey spectrum revealed typical peaks for Ce, S, C, O, and Ni components as shown in Fig. 2a, demonstrating that there is no other elemental impurity. At 248.7 eV, there was a clear C1s peak used to calibrate the position of the peaks present in the nanocomposite as shown in Fig. 2b. Figure 2c represents the O1s XPS spectrum where the peaks appeared at 533 and 531.5 eV which confirmed that it is the environmental oxygen which was adsorbed on the surface of the material from the environment. The XPS S2p spectrum is given in Fig. 2d and the peak that appeared at 169.7 eV confirmed that the sulfer is in a $-2$ oxidation state. Figure 2e depicts the bonding states of $Ce^{3+}$ and $Ce^{4+}$ coexist in this high-resolution spectrum. There are two deconvoluted peaks present in Ce3d5/2 at 886.7 eV and 905.01 eV confirming the $Ce^{3+}$, and the convolution peaks with binding energies at 900.1 eV, 906.9 eV, and 888.8 eV are used to represent the $Ce^{4+}$ states. The XPS Ni 2p spectrum has a good fit with the $Ni^{2+}$ valence state which is confirmed by their spin-orbital doublets (854.2, 873.3, and 879.1 eV) and shake-up satellites (860.9 and 879.78 eV). Deconvoluted Ni2p3/2 XPS

reveals nickel peaks in two distinct chemical states. There is a small peak at 852.79 eV, which corresponds to metallic Ni, while the two larger peaks at 855.5 and 856.7 eV, respectively, represent $Ni^{2+}$ as shown in Fig. 2f.

Scanning electron microscopy revealed a wide diversity of morphologies and architectures of all the synthesized products. Figure 3a depicts the morphological structures of CeS, indicating self-assembled nanowires. Figure 3b shows the NiS morphological architecture which is folded into two-dimensional sheets during the hydrothermal treatment. Finally, Fig. 3c represents the flower-like features with enhanced active sites and solid polyhedral nanostructures of the NiS/CeS nanocomposite. Figure 3d represents the transmission electron microscopy (TEM) to confirm the analysis for the internal textural formation of the nanocomposite (NiS/CeS), indicating that both phases were present in the prepared nanocomposite. The improved flower-like morphology with abundant active sites was responsible for the remarkable oxygen evolution reaction efficiency.

Nitrogen adsorption/desorption analysis was used to determine the surface area of the NiS, CeS, and NiS/CeS nanocomposites, as depicted in Fig. 3e–g. The specific surface areas of NiS, CeS, and NiS/CeS nanocomposite were computed using desorption curves and found to be 12.2 m² g⁻¹, 8.9 m² g⁻¹, and 18.14 m² g⁻¹, respectively. The higher the BET surface area of the nanocomposite responses, the greater efficiency of the synthesized materials due to enhanced surface-active sites of the electrocatalyst.
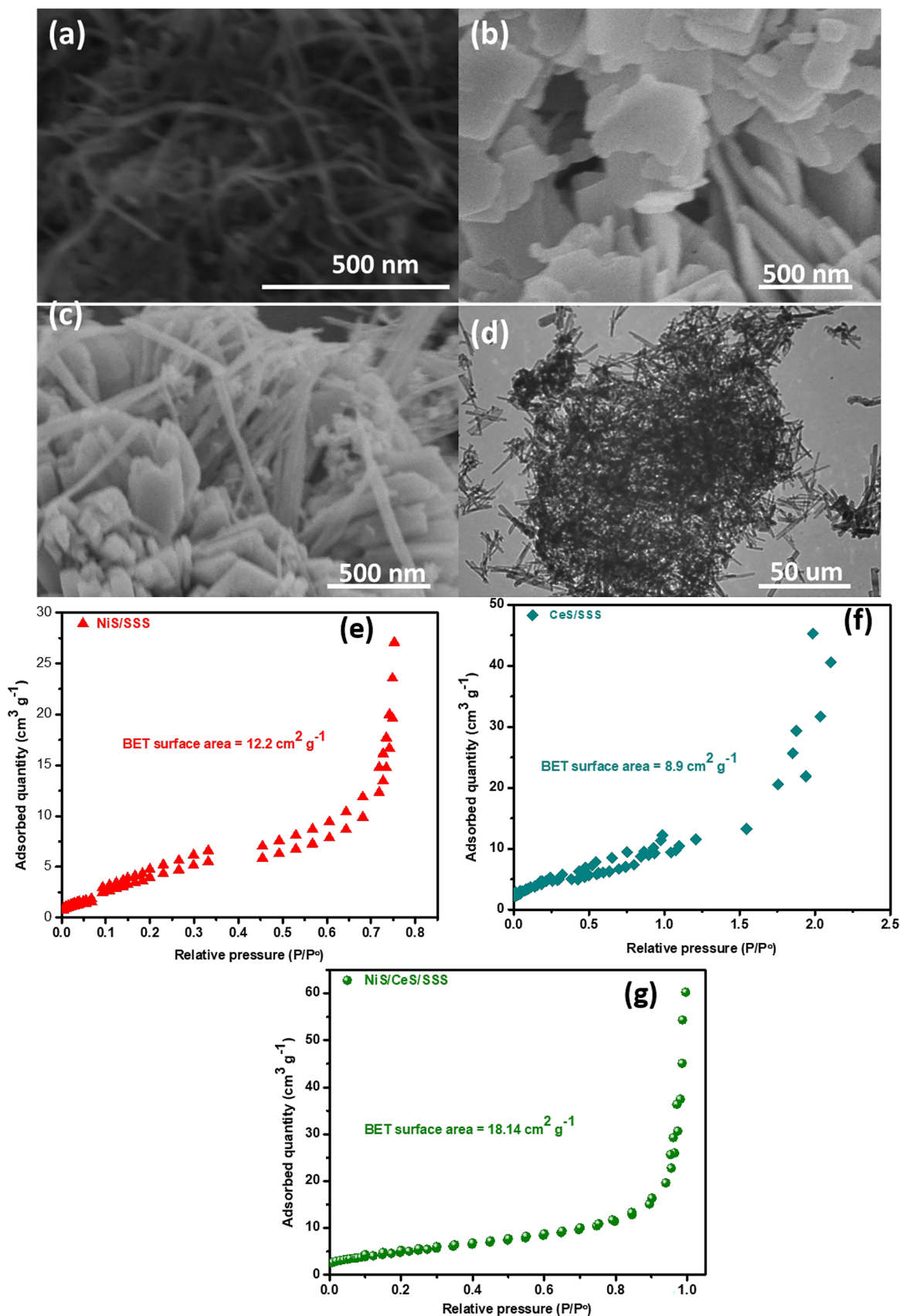
**Fig. 3** SEM images of **a** CeS, **b** NiS, **c** NiS/CeS, **d** TEM images of NiS/CeS, and **e**–**g** BET isotherm of NiS, CeS, and NiS/CeS nanocomposite
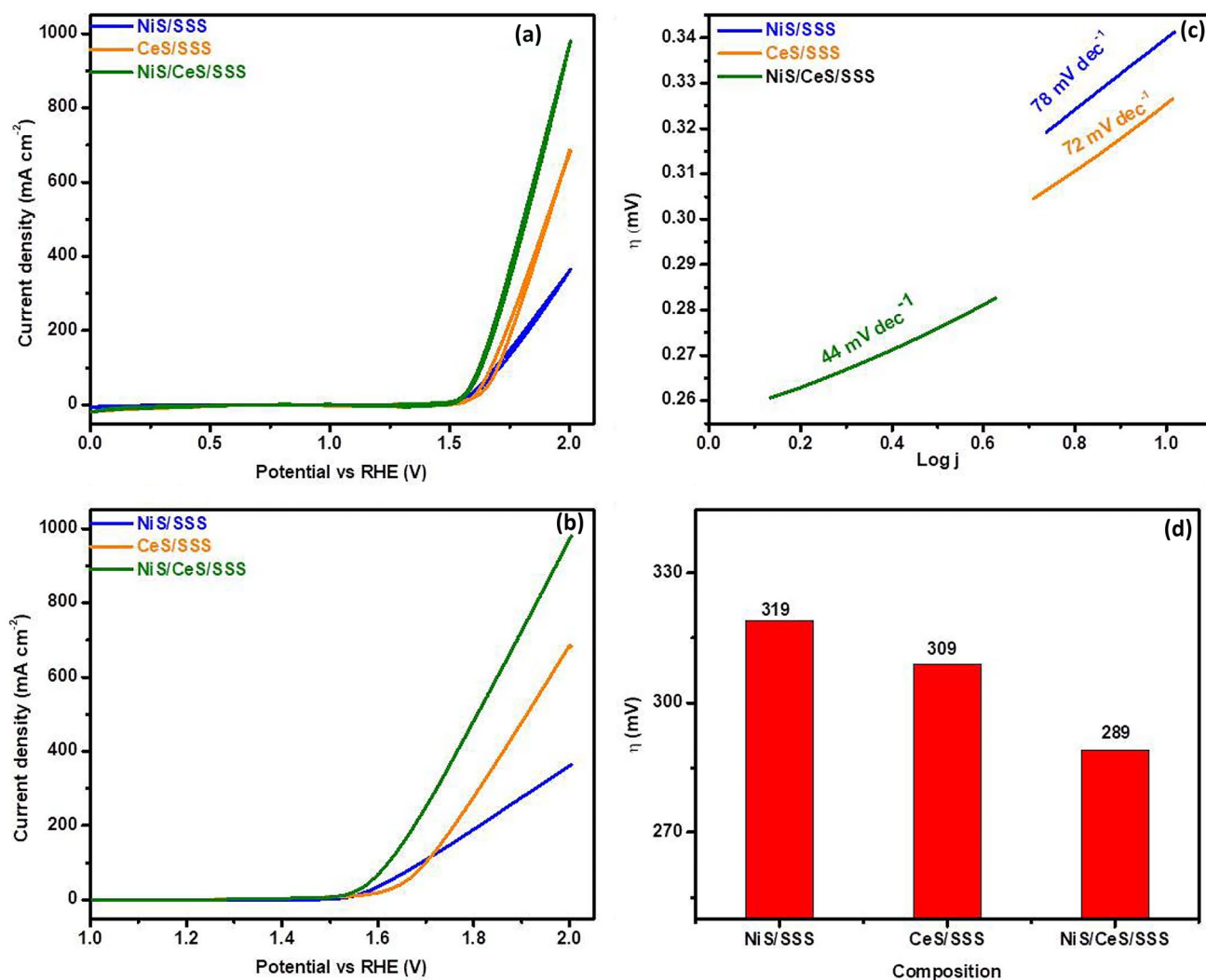
**Fig. 4** **a** CV, **b** LSV curves, **c** Tafel slope, and **d** comparison of overpotential of all the synthesized electrocatalysts
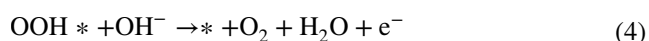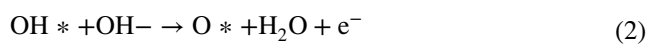
## Electrochemical performance

For electrochemical oxygen evolution reaction (OER) performance, the electrocatalytic efficiency of all the synthesized products has been investigated, and found that the composite materials worked exceptionally well. The best results were obtained with a 1:1 molar ratio of NiS/SSS and CeS/SSS in (1.0 M KOH) basic media at a scan rate of 5 mV s$^{-1}$. The cyclic voltammetry (CV) and linear sweep voltammetry (LSV) curves are shown in Fig. 4a, b. The sweep scans from numerous tries were collected to guarantee that the performed data was reproducible in 1.0 M KOH electrolyte in the potential range of 1 to − 1 V vs. RHE. The synthesized NiS/CeS/SSS electrocatalyst performed well with the lowest overpotential of 289 mV at 10 mA cm$^{-2}$, confirmed via cyclic and linear sweep voltammetry. Hence, the NiS/CeS/SSS electrocatalyst was better than the NiS (319 mV)

and CeS (309 mV), and the recently reported materials. The comparative study of the previously reported results has been tabulated in Table 1. Tafel plots obtained from CV and LSV curves were used to explore the kinetics and processes of OER for all the synthesized materials like NiS/SSS, CeS/SSS, and NiS/CeS/SSS nanocomposite. All the materials have different kinetic rates, i.e., the pure sample having the dynamic rates of 78 mV dec$^{-1}$ (NiS), 72 mV dec$^{-1}$ (CeS), and the nanocomposite having the highest kinetic rates of 44 mV dec$^{-1}$ as shown in Fig. 4c. In OER processes with four electrons, theoretical Tafel slopes of 40 mV dec$^{-1}$ correspond to a third charge transfer rate regulating phase. The decrease in the Tafel slope indicates that the OER surface-adsorbed species are still dominating, while the rise in the Tafel slope presents that the surface species formed in the step immediately preceding the rate-determining phase is decreasing. NiS/CeS/SSS nanocomposite has a lower Tafel

**Table 1** Comparative study of already reported results with the present study

| Sr. no | Electrocatalyst | Overpotential (mV) | Tafel slope (mVdec$^{-1}$) | Electrode material | Reference |
|---|---|---|---|---|---|
| 1 | $Fe_{0.95-x}Ni_xS_{1.05}$ | 228 | 53 | | [44] |
| 2 | $CoS_x/Ni_3S_2$@NF | 440@100 mAcm$^{-2}$ | 105.4 | Nickel foam (NF) | [45] |
| 3 | Ni/NiS | 340 | 109 | NF | [46] |
| 4 | $Ni_3S_2$ | 110 | 108 | NF | [47] |
| 5 | $Fe0.9Ni_2.1S_2$ | 252@100 mAcm$^{-2}$ | | NF | [48] |
| 6 | $Fe_{0.95-x}Ni_xS_{1.05}$ | 228 | 53 | NF | [44] |
| 7 | $Co_3Fe_7$@CNSs | 301 | 38.59 | Glassy carbon electrode (GCE) | [49] |
| 8 | $Bi_2S_3/Ni_3S_2$/NF | 268 | 82 | NF | [50] |
| 9 | Ni/g-$C_3N_4$@CuS | 600@15.5 | 68 | Indium tin oxide (ITO)–coated glass electrode | [51] |
| 10 | $Ni_3Se$ | 290 | 79.5 | - | [52] |
| 11 | $CoSe_2$ ultrathin nanosheets | 320 | 44 | - | [53] |
| 12 | Ag-$CoSe_2$ | 320 | 56 | - | [54] |
| 13 | $Ni_{0.5}Mo_{0.5}Se$ | 340 | | - | [55] |
| 14 | $NiCo_2Se_4$ | 295 | 53 | - | [56] |
| 15 | NiO/NiS | 209 mV | 60 mV dec$^{-1}$ | - | |
| 16 | $VO_x$/NiS/NF | 330 mV, 50 mA cm$^{-2}$ | 121 mV dec$^{-1}$ | NF | [57] |
| 17 | NiS@SLS | 297 mV | 47 mVdec$^{-1}$ | SLS (stainless steel) | [58] |
| 18 | NiS/$Fe_3O_4$@CNT | 243 mV | 44.2 mVdec$^{-1}$ | NF | [59] |
| 19 | NiS/CoS | 170 mV | 71 mVdec$^{-1}$ | NF | [60] |
| 20 | $Ni_3S_2$/NiS | 298 mV | 58.6 mV•dec$^{-1}$ | NF | [61] |
| **21** | **NiS/CeS/SSS** | **289** | **44** | **SSS** | **Present study** |

slope (44 mV dec$^{-1}$), indicating that the reactant (OH) is more readily adsorbed, implying a higher OER rate. The decrease in the Tafel slope and the overpotential values could be due to the synergistic effect between NiS/SSS and CeS/SSS. Figure 4d represents the overpotential comparison study of all the synthesized products. The four-step mechanism for the electrochemical OER process was discussed as:

$$OH^- + * \rightarrow OH* + e^- \tag{1}$$

$$OH* + OH- \rightarrow O* + H_2O + e^- \tag{2}$$

$$O* + OH- \rightarrow OOH* + e^- \tag{3}$$

$$OOH* + OH^- \rightarrow * + O_2 + H_2O + e^- \tag{4}$$

Cyclic voltammetry curves were used to assess the electrochemically active surface area of electrocatalysts to investigate their improved water oxidation activity, as depicted in Fig. 5a–c. A rough surface and many active sites influence the reaction's catalytic activity, resulting in an enhanced electrochemically active surface area (ECSA). The calculated $C_{dl}$ values for all the fabricated materials such as pure NiS/SSS, CeS/SSS, and NiS/CeS/SSS nanocomposite were 64 mF cm$^{-2}$, 50 mF cm$^{-2}$, and 77.5 mF cm$^{-2}$, respectively,

as shown in Fig. 5d–f. To calculate the ECSA, we normalized the $C_{dl}$ to the previously used specific capacitance (Cs) of 0.04 mF cm$^{-2}$ for a flat surface [62]. According to this study, the flower looks of the nanocomposite aids in the creation of a large number of active sites, which boosts the OER efficiency.

To better understand the charge transport process within the electrodes, electrochemical impedance spectra (EIS) were employed to analyze the synthesized samples. A semicircle follows a near-linear line in the high-frequency domain while in the low-frequency domain that bends toward the *x*-axis, as seen in Fig. 6a–d. Figure 6a represents the combined Nyquist plot of all the synthesized products. As shown in Fig. 6 (inset of b and d), an equivalent circuit can handle these designs. In most applications, the series resistance, abbreviated as Rs, is created by combining the contact resistance and the electrolyte resistance. The resistance to charge transfer (Rct) at the electrode/ electrolyte interface in the OER process is referred to as Rct. Due to the unequal distribution of active catalytic sites on the surface, constant phase elements are favored over the simple electrochemical process in actual EIS modeling circumstances. The resultant Nyquist plots with Rs and Rct values are depicted in Fig. 6b–d. Among all products, the nanocomposite has a more negligible charge
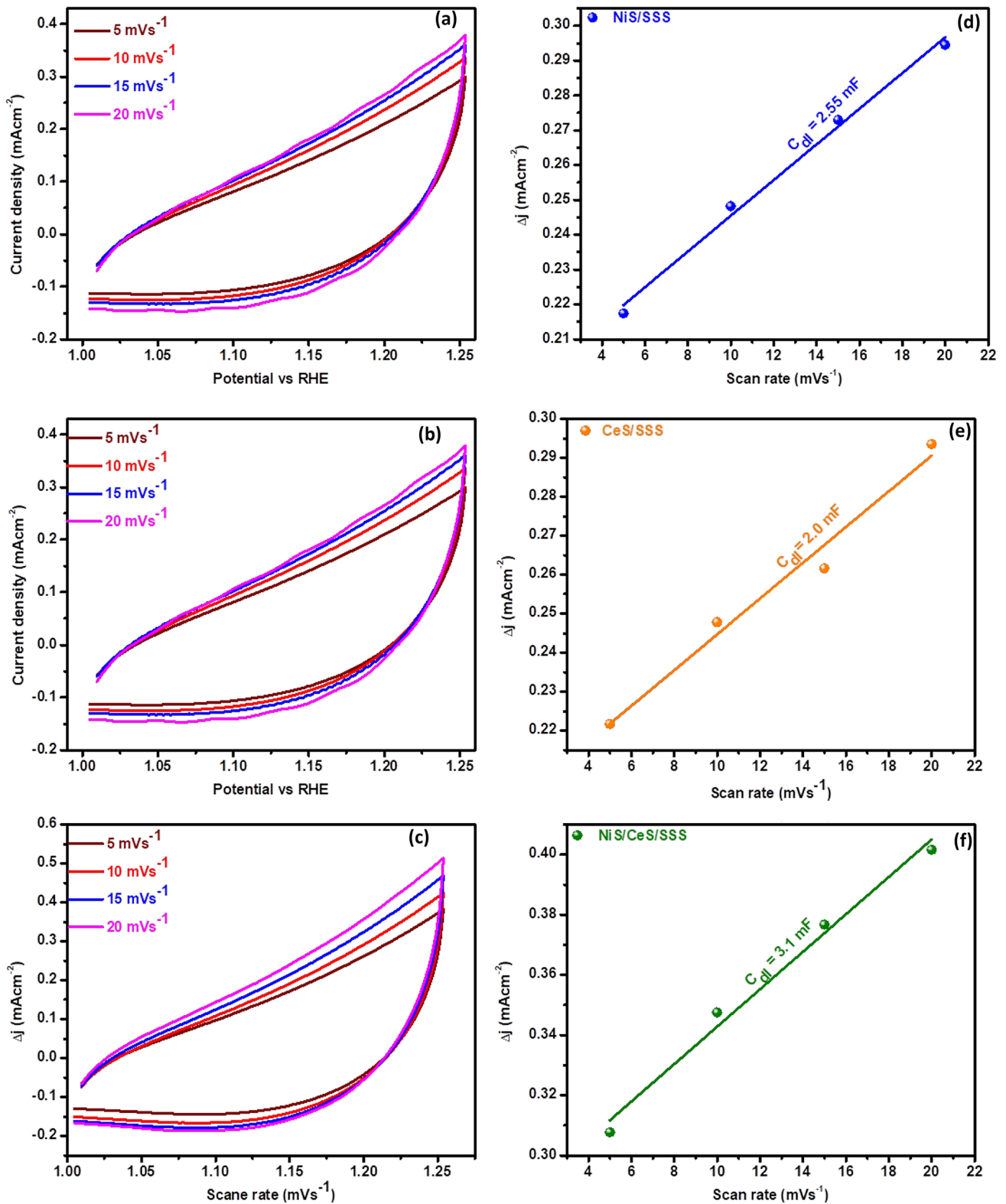
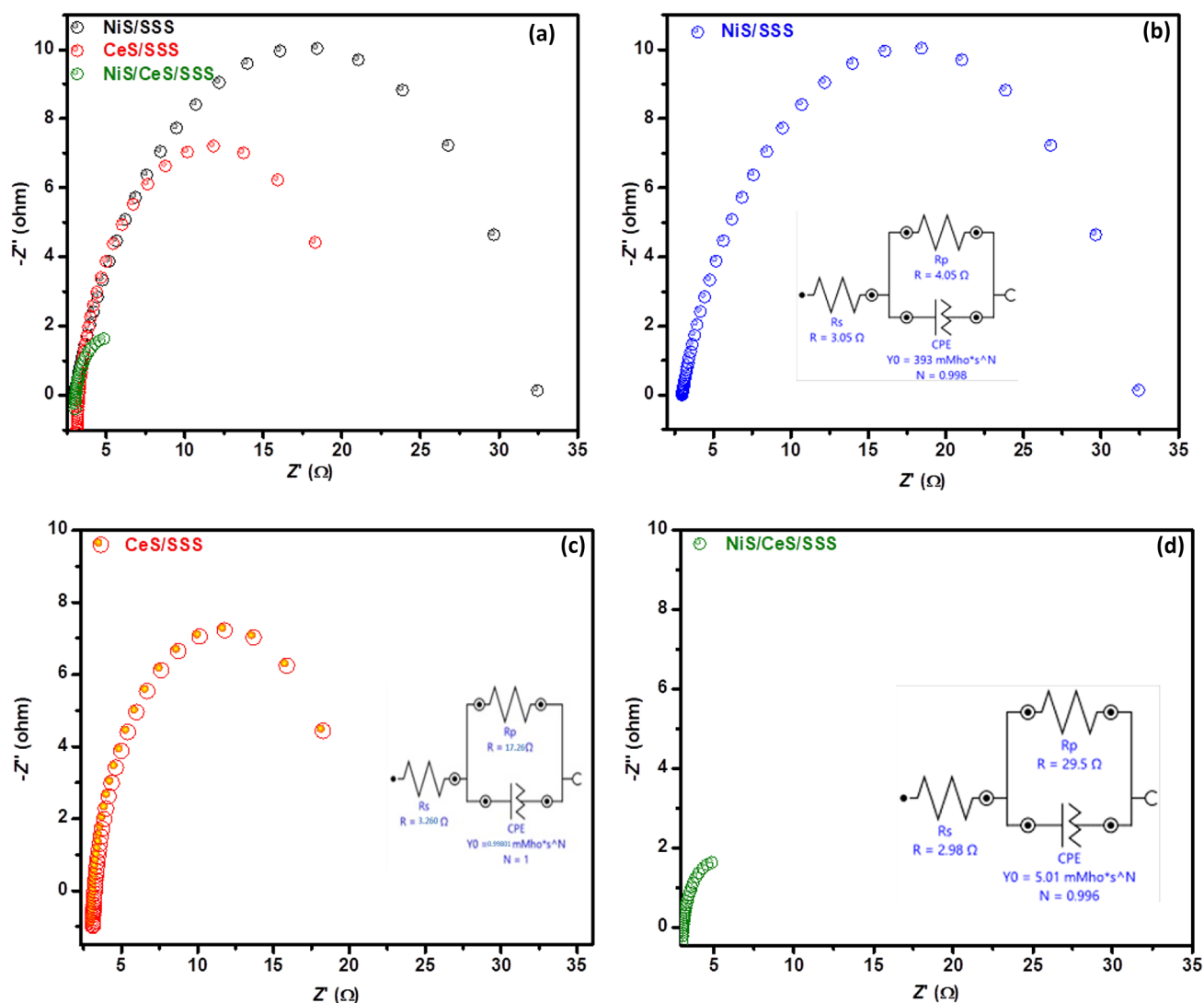**Fig. 5** **a–c** CV curves, **d–f** linear plot of change in current density vs. scan rate, respectively

**Fig. 6** **a** Combined Nyquist plot, **b–d** Nyquist plot with their fitted circuit for NiS/SSS, CeS/SSS, and NiS/CeS/SSS nanocomposite

transfer resistance. The smaller the Rct value, the higher will be the conductivity of the electrocatalyst.

Figure 7 depicts the stability tests of the NiS/CeS/SSS nanocomposite confirmed via cyclic voltammetry cycles (Fig. 7a) and chronoamperometry (Fig. 7b). After 1500 cycles, the CV curves show little change in the current density between the 1$^{st}$ and 1500$^{th}$ cycles, confirming the long-term stability. The chronoamperometric experiment also tested the electrocatalyst enduring. The electrode system that catalyzes the electrolysis of

water undergoes a 40-h stability test. The electrode's excellent catalytic stability, which shows its superior anti-corrosion qualities, allows it to be used during water electrolysis. Finally, the XRD pattern of the used electrocatalyst was also performed, to confirm the stability in the structure of the NiS/CeS/SSS nanocomposite as shown in Fig. 7c. The resultant pattern showed that there are no phase changes after long-term stability in alkaline media which again confirmed its stability in terms of its structure.
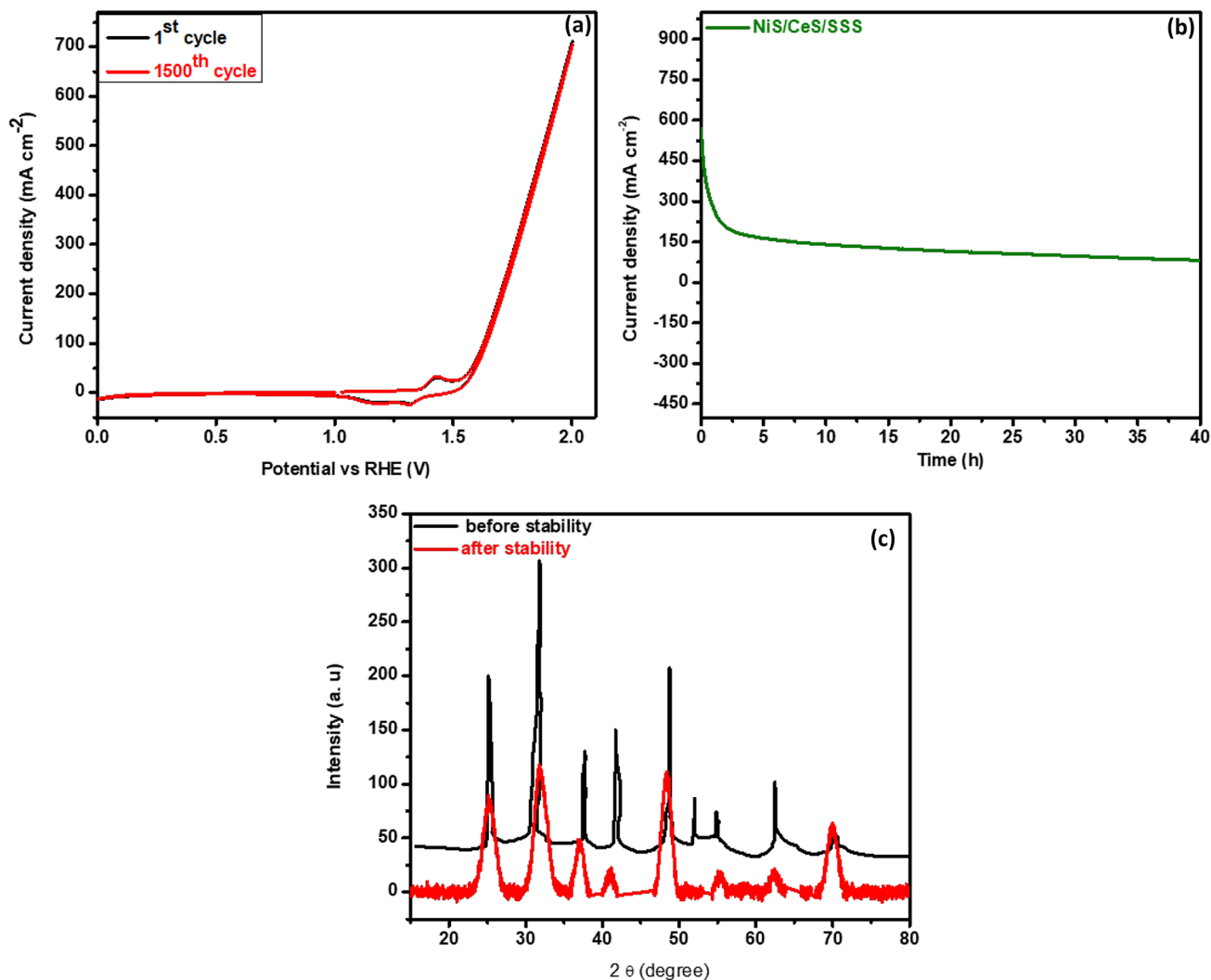
**Fig. 7** **a** Stability cycles, **b** chronoamperometry of the synthesized NiS/CeS/SSS nanocomposite, and **c** comparison of XRD before and after stability

## Conclusion

A simple hydrothermal procedure was used to successfully create NiS/SSS, CeS/SSS, and NiS/CeS/SSS nanocomposite. All the fabricated materials are analyzed via different analytical techniques to confirm their formation. The present study describes an oxygen evolution reaction using all the synthesized materials as working electrodes performing effectively in alkaline media. To attain a current density of 10 mA cm$^{-2}$, a low overpotential of 289 mV is needed with a low Tafel slope of 44 mV dec$^{-1}$ for easy electron transfer reaction. The extraordinary performance of water electrolysis is due to the flower-like morphology, high surface area, and enhanced electrochemical surface-active sites of the samples.

## References

1. Gansukh Z (2021) Mongol dream beyond fossil fuels: prosperity of greenification. Renew Energy 171:95–102
2. Baum CM, Low S, Sovacool BK (2022) Between the sun and us: expert perceptions on the innovation, policy, and deep uncertainties of space-based solar geoengineering. Renew Sustain Energ Rev 158:112179

3. Holden E, Linnerud K, Rygg BJ (2021) A review of dominant sustainable energy narratives. Renew Sustain Energ Rev 144:110955

4. Chen Z, Wei W, Ni BJ (2021) Cost-effective catalysts for renewable hydrogen production via electrochemical water splitting: recent advances. Curr Opin in Green Sustain Chem 27:100398

5. Upadhyay SN, Pakhira S (2022) Electrochemical water splitting: $H_2$ evolution reaction. Photoelectrochem Hydrog Gen 59–89

6. Li X, Zhao L, Yu J, Liu X, Zhang X, Liu H, Zhou W (2020) Water splitting: from electrode to green energy system. Nano-Micro Letters 12(1):1–29

7. Qadir SA, Al-Motairi H, Tahir F, Al-Fagih L (2021) Incentives and strategies for financing the renewable energy transition: a review. Energy Rep 7:3590–3606

8. Al-Madanat O, Curti M, Gunnemann C, AlSalka Y, Dillert R, Bahnemann DW (2021) $TiO_2$ photocatalysis: impact of the platinum loading method on reductive and oxidative half-reactions. Catal 380:3–15

9. Hojamberdiev M, Vargas R, Kadirova ZC, Kato K, Sena H, Krasnov AG, Yamakata A, Teshima K, Lerch M (2022) Unfolding the role of B site-selective doping of aliovalent cations on enhancing sacrificial visible light-induced photocatalytic H2 and O2 evolution over BaTaO2N. ACS Catal 12:1403–1414

10. Zhao L, Yu G, Huang X, Chen W (2022) Realizing efficient catalytic performance and high selectivity for oxygen reduction reaction on a 2D $Ni_2SbTe_2$ monolayer. Inorg 61:2284–2291

11. Wang J, Hu H, Lu S, Hu J, Zhu H, Duan F, Du M (2022) Conductive metal and covalent organic frameworks for electrocatalysis: design principles, recent progress, and perspective. Nanoscale 14:277–288

12. Kou T, Wang S, Li Y (2021) Perspective on high-rate alkaline water splitting. ACS Mater Lett 3:224–234

13. Yao D, Gu L, Zuo B, Weng S, Deng S, Hao W (2021) A strategy for preparing high-efficiency and economic catalytic electrodes toward overall water splitting. Nanoscale 13:10624–10648

14. Wang W, Wang W, Ren X, Liu X, Li Z (2021) Synthesis of Ni3S4/NiS2/FeS2 nanoparticles for hydrogen and oxygen evolution reaction. Appl surf Sci 560:149985

15. Wang W, Xu Y, Yao J, Liu X, Yen Z, Li Z (2020) Enhanced oxygen and hydrogen evolution performance by carbon-coated CoS 2–FeS 2 nanosheets. Dalton trans 49:13352–13358

16. Li J (2022) Oxygen Evolution Reaction in Energy Conversion and Storage: Design Strategies Under and Beyond the Energy Scaling Relationship. Nano-Micro Letters 14(1):1–32

17. Arunachalam P, Senthil C, Elumalai G (2022) Nanostructured nonoxide nanomaterials an introduction, in Oxide Free Nanomaterials for Energy Storage and Conversion Applications. Elsevier 1–24

18. Kao WC, Northumberland COP, Cheng TC, Ortiz J, Durand A, Loeffelholz OV, Schilling O, Biniossek ML, Klaholz BP, Hunte C (2022) Structural basis for safe and efficient energy conversion in a respiratory supercomplex. Nat Commun 13:1–12

19. Novoselova A, Smolenski V, Volkovich VA, Ryzhov AA, Yan Y, Xue Y, Ma F (2022) Electrode processes and electrochemical formation of Dy-Ga and Dy-Cd alloys in molten LiCl–KCl–CsCl eutectic. J Electroanal Chem 906:116012

20. Mohideen MM, Radhamani AV, Ramakrishna S, Wei Y, Liu Y (2022) Recent insights on iron-based nanostructured electrocatalyst and the current proton exchange membrane fuel cell status for sustainable transport. J Energy Chem In Press

21. Li Q, Wang YW, Zeng J, Zhao X, Chen C, Wu QM, Chen LM, Chen ZY, Lei YP (2021) Bimetallic chalcogenides for electrocatalytic CO2 reduction. Rare Met 40:3442–3453

22. Sajjad M, Amin M, Javed MS, Imran M, Hu W, Mao Z, Lu W (2021) Recent trends in transition metal diselenides (XSe2: X= Ni, Mn, Co) and their composites for high energy faradic supercapacitors. J Energy Storage 43:103176

23. Pham DT, Quan T, Mei S, Lu Y (2022) Colloidal metal sulfide nanoparticles for high-performance electrochemical energy storage systems. Curr Opin in Green Sustain Chem 34:100596

24. Hussain I, Sahoo S, Lamiel C, Nguyen TT, Ahmed M, Xi C, Iqbal S, Ali A, Abbas A, Javed MS, Zhang K (2022) Research progress, and future aspects: metal selenides as effective electrodes. Energy Storage Mat 47:13–43

25. Iqbal MZ, Aziz U (2022) Supercapattery: merging of battery-supercapacitor electrodes for hybrid energy storage devices. J Energy Storage 46:103823

26. Shaikh NS, Ubale SB, Mane VJ, Shaikh JS, Lokhande VC, praserthdam S, Lokhande CD, Kanjanaboos P (2022) Novel electrodes for supercapacitor: conducting polymers, metal oxides, chalcogenides, carbides, nitrides, MXenes, and their composites with graphene. J Alloys Compd 893:161998

27. Şenocak A, Korkmaz E, Khataee A, Demirbas E (2022) A facile and synergetic strategy for electrochemical sensing of rutin antioxidant by Ce–Cr doped magnetite@ rGO. Mater Chem Phys 275:125298

28. Shen M, Ai F, Ma H, Xu H, Zhang Y (2021) Progress and prospects of reversible solid oxide fuel cell materials. IScience 24:103464

29. Sajjad M, Khan MI, Cheng f, Lu W (2021) A review on selection criteria of aqueous electrolytes performance evaluation for advanced asymmetric supercapacitors. J Energy Storage 40:102729

30. Majumdar D, Ghosh S (2021) Recent advancements of copper oxide-based nanomaterials for supercapacitor applications. J Energy Storage 34:101995

31. Khan I, Baig N, Ali S, Usman M, Khan SA, Saeed K (2021) Progress in the layered cathode and anode nanoarchitectures for charge storage devices: challenges and future perspective. Energy Storage Mater 35:443–469

32. Nikodimos Y, Huang CJ, Taklu BW, Su WN, Hwang BJ (2022) Chemical stability of sulfide solid-state electrolytes: stability toward humid air and compatibility with solvents and binders. Energy Environ Sci In Press

33. Pramitha A, Raviprakash Y (2022) Recent developments and viable approaches for high-performance supercapacitors using transition metal-based electrode materials. J Energy Storage 49:104120

34. Zhang Y, Chao S, Wang X, Han H, Bai Z, yang L (2017) Hierarchical Co9S8 hollow microspheres as multifunctional electrocatalysts for oxygen reduction, oxygen evolution, and hydrogen evolution reactions. Electrochim Acta 246:380–390

35. Qi Y, Wu J, Xu J, Gao H, Du Z, Liu B, Liu L, Xiong D (2020) One-step fabrication of a self-supported Co@ CoTe 2 electrocatalyst for efficient and durable oxygen evolution reactions. Inorg Chem Front 7:2523–2532

36. Sun Y, Zhang T, Li C, Xu K, Li Y (2020) Compositional engineering of sulfides, phosphides, carbides, nitrides, oxides, and hydroxides for water splitting. J Mater Chem A 8:13415–13436

37. Zhang J, Wang T, Pohl D, Rellinghaus B, Dong R, Liu S, Zhauang X, Feng X (2016) Interface engineering of MoS 2/Ni 3 S 2 heterostructures for highly enhanced electrochemical overall-water-splitting activity. Angew Chem Int Ed 55:6702–6707

38. Gong Y, Lin Y, Yang Z, Jiao F, Li J, Wang W (2019) High-performance bifunctional flower-like Mn-doped Cu7. 2S4@ NiS2@ NiS/NF catalyst for overall water splitting. Appl Surf Sci 476:840–849

39. Srinivas K, Chen Y, Wang X, Wang B, Karpuraranjith M, Wang W, Su Z, Zhang W, Yang D (2021) Constructing Ni/NiS heteronanoparticle-embedded metal-organic framework-derived nanosheets for enhanced water-splitting catalysis. ACS Sustain Chem Eng 4:1920–1931

40. Wang N, Wang J, Liu M, Ge C, Hou B, Liu N, Ning Y, Hu Y (2021) Preparation of FeS2/TiO2 nanocomposite films and study

on the performance of photoelectrochemistry cathodic protection. Sci Rep 11:1–12

41. Zhang L, Zhao H, Xu S, Liu Q, Li T, Luo Y, Gao S, Shi X, Asiri MA, Sun X (2021) Recent advances in 1D electrospun nano-catalysts for electrochemical water splitting. Small Structures 2:2000048

42. Nakayasu Y, Kobayashi H, Katahira S, Tomai T, Honma I (2022) Rapid, one-step fabrication of MoS2 electrocatalysts by hydrothermal electrodeposition. Electrochem Commun 134:107180

43. Jing Z, Zhao Q, Zheng D, Sun L, Geng J, Zhou Q, Lin J (2020) Nickel-doped pyrrhotite iron sulfide nanosheets as a highly efficient electrocatalyst for water splitting. J Mater Chem A 8:20323–20330

44. Shit S, Chhetri S, Jang W, Murmu NC, Koo H, Samanta P, Kuila T (2018) Cobalt sulfide/nickel sulfide heterostructure directly grown on nickel foam: an efficient and durable electrocatalyst for overall water splitting application. ACS Appl Mater interf 10:27712–27722

45. Hegazy MBZ, Mohamed RB, Yamauchi Y, Pakdel A, Cao R, Apfel U (2021) Synergistic electrocatalytic hydrogen evolution in Ni/NiS nanoparticles wrapped in multi-heteroatom-doped reduced graphene oxide Nanosheets. ACS Appl Mater Interfaces 13:34043–34052

46. Chen P (2017) 3D nitrogen-anion-decorated nickel sulfides for highly efficient overall water splitting. J Adv Mater 29:1701584

47. Fei B, Chen Z, Liu J, Xu H, Yan X, Qing H, Chen M, Wu R (2020) Ultrathinning nickel sulfide with modulated electron density for efficient water splitting. Adv Energy Mater 10:2001963

48. Liu C, Jia D, Hao Q, Zheng X, Li Y, Tang C, Liu H, Zhang J, Zheng X (2019) P-doped iron–nickel sulfide nanosheet arrays for highly efficient overall water splitting. ACS Appl Mater Interfaces 11:27667–27676

49. Yaseen W, Ullah N, Xie M, Wei W, Xu Y, Zahid M, Oluigbo CJ, Yusuf BA, Xie J (2021) Cobalt–iron nanoparticles encapsulated in mesoporous carbon nanosheets: a one-pot synthesis of highly stable electrocatalysts for overall water splitting. Int J Hydrog Energy 46:5234–5249

50. Wang S, Xue W, Fang Y, Li Y, Wang W, Zhao R (2020) Bismuth activated succulent-like binary metal sulfide heterostructure as a binder-free electrocatalyst for enhanced oxygen evolution reaction. J Colloid Interface Sci 573:150–157

51. Chaudhary P, Ingole PP (2020) Nickel incorporated graphitic carbon nitride supported copper sulfide for efficient noble-metal-free photo-electrochemical water splitting. Electrochim Acta 357:136798

52. Sweis AT, Masud J, Nath M (2016) Nickel selenide as a high-efficiency catalyst for oxygen evolution reaction. Energy Environ Sci 9:1771–1782

53. LiuY CH, Lyu M, Fan S, Liu Q, Zhang W, Zhi Y, Wang C, Xiao C, Wei S, Ye B, Xie Y (2014) Low overpotential in vacancy-rich ultrathin CoSe2 nanosheets for water oxidation. J Am Chem Soc 136:15670–15675

54. Zhao X, Zhang H, Yan Y, Cao J, Li X, Zhou S, Peng Z, Zeng J (2017) Engineering the electrical conductivity of lamellar silver-doped cobalt (II) selenide nanobelts for enhanced oxygen evolution. Angew Chem 129:334–338

55. Premnath K, Arunachalam P, Amer MS, Madhavan J, Al-Mayouf AM (2019) Hydrothermally synthesized nickel molybdenum selenide composites as cost-effective and efficient trifunctional electrocatalysts for water splitting reactions. Int J Hydrog Energy 44:22796–22805

56. Ming F, Liang H, Shi H, Mei G, Wang Z (2016) MOF-derived Co-doped nickel selenide/C electrocatalysts supported on Ni foam for overall water splitting. J Mater Chem A 4:15148–15155

57. Chai YM, Zhang XY, Lin JH, Qin JF, Liu ZZ, Xie JY (2019) Three-dimensional VOx/NiS/NF nanosheets as efficient electrocatalyst for oxygen evolution reaction. Int J Hydrog Energy 21:10156–10162

58. Chen JS, Ren J, Shalom M, Fellinger T, Antonietti M (2016) Stainless steel mesh-supported NiS nanosheet array as highly efficient catalyst for oxygen evolution reaction. ACS appl Mat interfaces 8:5509–5516

59. Srinivas K, Chen Y, Wang B, Yu B, Wang X, Hu Y (2020) Metal–organic framework-derived NiS/Fe3O4 heterostructure-decorated carbon nanotubes as highly efficient and durable electrocatalysts for oxygen evolution reaction. ACS Appl Mater Interfaces 28:31552–31563

60. Ma Z, Zhao Q, Li J, Tang B, Zhang Z, Wang X (2018) Three-dimensional well-mixed/highly-densed NiS-CoS nanorod arrays: an efficient and stable bifunctional electrocatalyst for hydrogen and oxygen evolution reactions. Electrochem Acta 260:82–91

61. Wang J, Zeng H (2019) A hybrid electrocatalyst with a coordinatively unsaturated metal–organic framework shell and hollow Ni3S2/NiS core for oxygen evolution reaction applications ACS APPl Mater Interface Sci 26:23180–23191

62. McCrory CC, Jung S, Ferrer IM, Chatman SM, Peters JC, Jaramillo TF (2015) Benchmarking hydrogen evolving reaction and oxygen evolving reaction electrocatalysts for solar water splitting devices. J Am Chem Soc 137:4347–4357